

1 **Bispecific antibody prevents SARS-CoV-2 escape and protects mice from** 2 **disease**

3
4 Raoul De Gasparo^{a,#}, Mattia Pedotti^{a,#}, Luca Simonelli^a, Petr Nickl^b, Frauke Muecksch^h, Julio C.
5 C. Lorenziⁱ, Federica Mazzola^a, Davide Magri^j, Tereza Michalcikova^b, Jan Haviernik^c, Vaclav
6 Honig^{c,d}, Irene Cassaniti^k, Elena Percivalle^k, Blanka Mrazkova^b, Natalie Polakova^b, Andrea
7 Fortova^c, Jolana Tureckova^b, Veronika Iatsiuk^b, Salvatore Di Girolamo^a, Martin Palus^{c,d}, Dagmar
8 Zudova^b, Petr Bednar^{c,e}, Ivana Bukova^b, Filippo Bianchini^a, Dora Mehnⁱ, Radim Nencka^f, Petra
9 Strakova^c, Oto Pavlis^g, Jan Rozman^b, Sabrina Gioria^j, José Camilla Sammartino^k, Federica
10 Giardina^k, Stefano Gaiarsa^k, Qiang Pan Hammarström^m, Christopher O. Barnesⁿ, Antonio
11 Piralla^k, Pamela J. Bjorkmanⁿ, Fausto Baldanti^k, Luigi Calzolari^j, Michel C. Nussenzweig^{i,l}, Paul
12 D. Bieniasz^{h,l}, Theodora Hatziioannou^h, Jan Prochazka^b, Radislav Sedlacek^b, Davide F.
13 Robbiani^{a*}, Daniel Ruzek^{c,d*}, Luca Varani^{a*}.

14
15 ^a Institute for Research in Biomedicine, Università della Svizzera italiana (USI), Bellinzona,
16 Switzerland

17 ^b Czech Centre of Phenogenomics, Institute of Molecular Genetics of the Czech Academy of
18 Sciences, Vestec, Czech Republic.

19 ^c Veterinary Research Institute, Brno, Czech Republic

20 ^d Institute of Parasitology, Biology Centre of the Czech Academy of Sciences, Ceske
21 Budejovice, Czech Republic

22 ^e Faculty of Science, University of South Bohemia, Ceske Budejovice, Czech Republic

23 ^f Institute of Organic Chemistry and Biochemistry of the Czech Academy of Sciences, Prague,
24 Czech Republic

25 ^g Center of Biological Defense, Military Health Institute, Military Medical Agency, Techonin,
26 Czech Republic

27 ^h Laboratory of Retrovirology, The Rockefeller University, New York, NY, USA

28 ⁱ Laboratory of Molecular Immunology, The Rockefeller University, New York, NY, USA

29 ^j European Commission, Joint Research Centre, Ispra, VA, Italy

30 ^k Molecular Virology Unit, Microbiology and Virology Department, Fondazione IRCCS
31 Policlinico San Matteo, Pavia, Italy

32 ^l Howard Hughes Medical Institute, The Rockefeller University, New York, NY, USA

33 ^m Department of Biosciences and Nutrition, Karolinska Institutet, SE14183, Huddinge, Sweden

34 ⁿ Division of Biology and Biological Engineering, California Institute of Technology, Pasadena,
35 CA, USA

36
37 [#] These authors contributed equally

38 ^{*} Corresponding authors

39

40

41 **Summary**

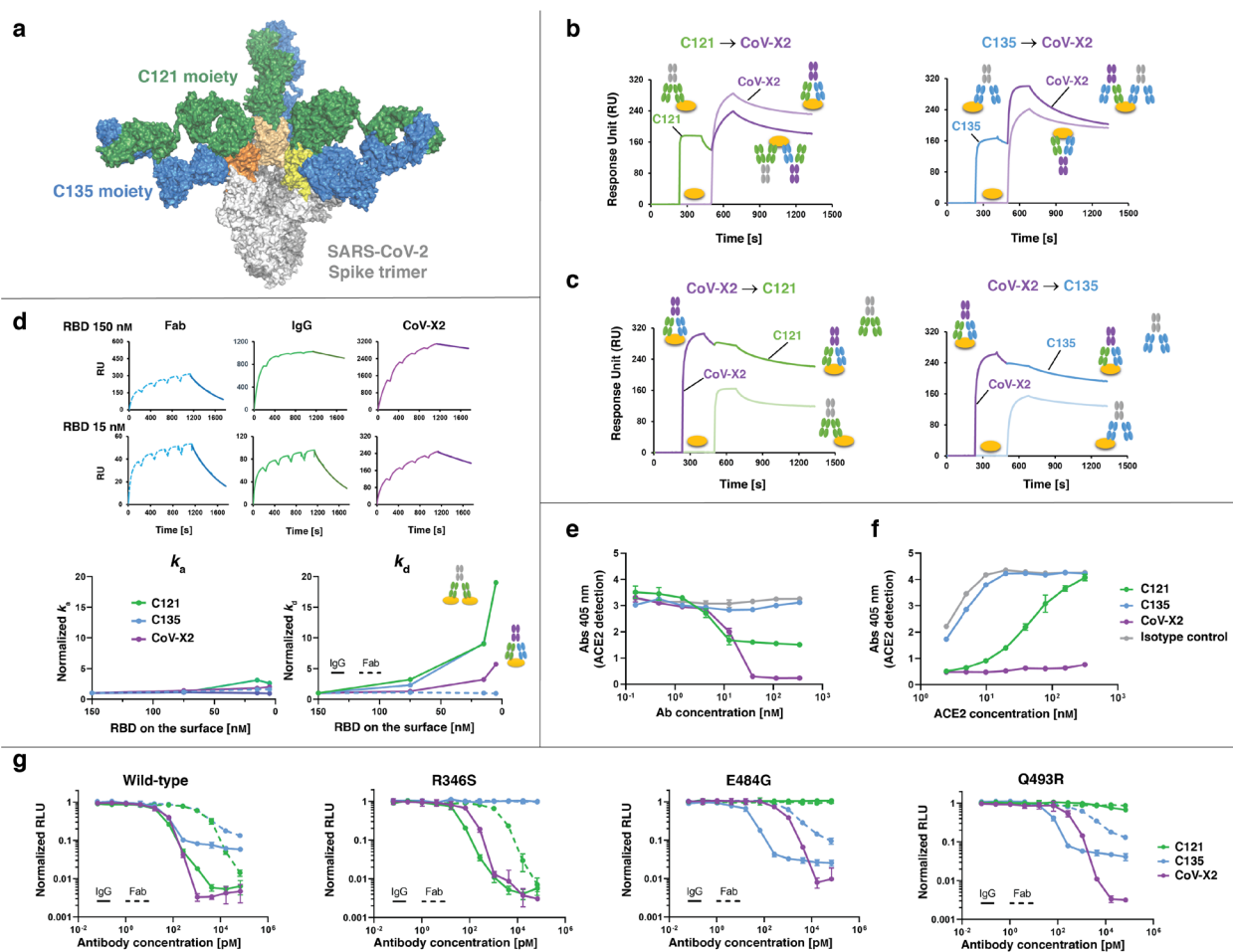
42 Neutralizing antibodies targeting the receptor binding domain (RBD) of the SARS-CoV-2 Spike
43 (S) are among the most promising approaches against coronavirus disease 2019 (COVID-19)^{1,2}.
44 We developed a bispecific, IgG1-like molecule based on two antibodies derived from COVID-19
45 convalescent donors, C121 and C135³. CoV-X2 simultaneously binds two independent sites on
46 the RBD and, unlike its parental antibodies, completely prevents S binding to Angiotensin-
47 Converting Enzyme 2 (ACE2), the virus cellular receptor. Furthermore, CoV-X2 recognizes a
48 broad panel of RBD variants and neutralizes SARS-CoV-2 and the escape mutants generated by
49 the single monoclonals at sub-nanomolar concentrations. In a novel model of SARS-CoV-2
50 infection with lung inflammation, CoV-X2 protects mice from disease and suppresses viral escape.
51 Thus, simultaneous targeting of non-overlapping RBD epitopes by IgG-like bispecific antibodies
52 is feasible and effective, combining into a single molecule the advantages of antibody cocktails.

53

54 The COVID-19 pandemic prompted an unprecedented effort to develop effective countermeasures
55 against SARS-CoV-2. Pre-clinical data and phase III clinical studies indicate that monoclonal
56 antibodies (mAbs) could be effectively deployed for prevention or treatment during the viremic
57 phase of the disease^{1,2}. Cocktails of two or more mAbs are preferred over a single antibody for
58 increased efficacy and prevention of viral escape, but this approach increases manufacturing
59 volumes and costs, complicates formulation^{4,5} and hinders novel strategies like antibody delivery
60 by viral vectors or by non-vectored nucleic acids⁶⁻⁸. Instead, multispecific antibodies embody the
61 advantages of a cocktail within a single molecule.

62 To this avail, we employed structural information⁹ and computational simulations to design
63 bispecifics that would simultaneously bind to (i) independent sites on the same RBD and (ii)
64 distinct RBDs on a S trimer. Out of several designs evaluated by atomistic Molecular Dynamics
65 simulations, 4 were produced and CoV-X2 was the most potent neutralizer of SARS-CoV-2
66 pseudovirus (half-maximal inhibitory concentration (IC_{50}) = 0.04 nM (5.8 ng/mL); Extended Data
67 Fig.1). CoV-X2 is a human-derived, CrossMAb-format IgG1-like bispecific antibody¹⁰ resulting
68 from the combination of the Fragment antigen binding (Fab) of mAbs C121 and C135, two potent
69 SARS-CoV-2 neutralizers³. Structural predictions showed that CoV-X2, but not its parental
70 monoclonals, can bind bivalently to all RBD conformations on the S trimer, preventing ACE2
71 access (Fig.1a and Extended Data Fig.2)¹¹.

72 CoV-X2 bound to RBD (K_D = 2.3 nM), S trimer (K_D = 0.2 nM), and to several S trimer
73 mutants, including the naturally occurring D614G, residues mutated or adjacent to those mutated
74 in the novel United Kingdom (202012/01 or B.1.1.7; N501Y) and South African variants
75 (501Y.V2; K417N, E484K and N501Y)^{12,13}, and the escape mutants of the parental mAbs¹⁴
76 (Extended Data Figs.3 and 4).

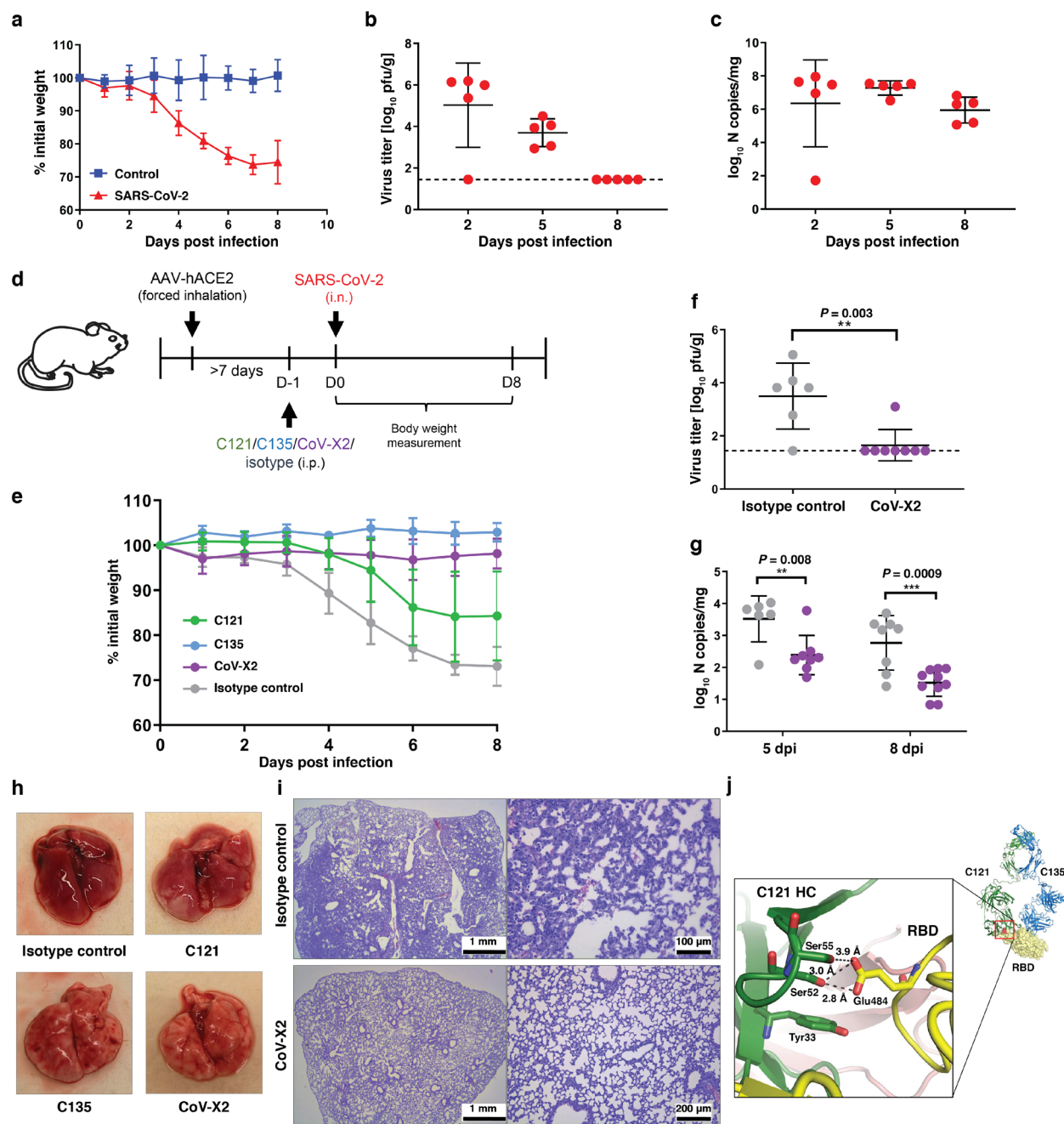


77
 78 **Fig.1 | Biochemical and *in vitro* neutralizing properties of CoV-X2 are superior to its parental mAbs.**
 79 **a**, Computational simulations predict bivalent binding of CoV-X2 to all three RBDs on the S trimer (see
 80 also Extended Data Fig.2). Green and blue are C121 and C135 moieties, respectively; RBDs are in shades
 81 of yellow/orange. **b**, **c**, SPR demonstrates that both arms of CoV-X2 are functional. In (**b**), immobilized
 82 RBD complexed with the indicated mAb (first antibody) binds to CoV-X2 (second antibody). In (**c**), the
 83 RBD/CoV-X2 complex prevents binding by the single mAbs. Shaded colors are controls (second antibody
 84 only). **d**, Both arms of CoV-X2 bind simultaneously to the RBD since, contrary to the monoclonals, avidity
 85 is retained at decreasing RBD concentrations. On top, representative SPR traces indicating the different
 86 dissociations of antibodies (or Fab) binding to RBD immobilized at different concentrations on the SPR
 87 chip (see also Extended Data Fig.5). At the bottom, plots of the normalized k_a and k_d values obtained with
 88 different concentrations of immobilized RBD. Increasing normalized dissociation rate (k_d) values indicate
 89 loss of avidity. **e**, **f**, CoV-X2 fully prevents ACE2 binding to S trimer in ELISA. ACE2 binding to
 90 antibody/S trimer complexes is measured either with increasing concentration of the indicated antibody and
 91 constant ACE2 (**e**), or at constant antibody concentration with increasing ACE2 (**f**). Mean with standard
 92 deviation of two experiments is shown. **g**, CoV-X2 neutralizes SARS-CoV-2 pseudovirus and escape
 93 mutants of its parental mAbs. Normalized relative luminescence (RLU) for cell lysates after infection with
 94 nanoluc-expressing SARS-CoV-2 pseudovirus in the presence of increasing concentrations of antibodies.
 95 Wild type SARS-CoV-2 pseudovirus (left) is shown alongside three escape mutants generated in the
 96 presence of C121 or C135¹⁴. Dashed lines are parental Fabs. Mean with standard deviation; one of two
 97 independent experiments.

98 CoV-X2 also bound to pre-formed C121/RBD and C135/RBD complexes, thus confirming
99 that both of its arms are functional (Fig.1b,c). Next, an avidity assay by Surface Plasmon
100 Resonance (SPR) was used to experimentally confirm the computational prediction that CoV-X2
101 can simultaneously engage two sites on the same RBD (Methods, Fig.1d and Extended Data Fig.5).
102 Avidity occurs when IgGs bind bivalently to antigens, resulting in slower dissociation rates (k_d)
103 (Extended Data Fig.5a). Accordingly, C121 and C135 IgG showed avidity at high antigen
104 concentrations due to intermolecular binding of adjacent RBDs; at lower antigen concentrations
105 the dissociation rate was instead faster since intermolecular binding was prevented by the increased
106 distance between RBD molecules, resulting in loss of avidity. Intramolecular avidity is not possible
107 for C121 and C135 since a single epitope is available on each RBD molecule. By contrast, CoV-
108 X2 maintained avidity even at low antigen concentrations, indicating bivalent, intramolecular
109 binding (Fig.1d and Extended Data Fig.5). ELISA assays were then performed to evaluate the
110 ability of CoV-X2 to inhibit the binding of recombinant ACE2 to the S trimer (Fig.1e,f). In line
111 with the structural information⁹, C135 did not affect the ACE2/S interaction. C121, which occupies
112 the ACE2 binding site on the RBD, prevented ACE2 binding but only partially. By contrast,
113 complete inhibition of ACE2 binding was synergistically achieved in the presence of CoV-X2.

114 To assess the neutralizing ability of CoV-X2 *in vitro*, we used SARS-CoV-2
115 pseudoviruses¹⁵. The bispecific neutralized pseudovirus carrying wild type SARS-CoV-2 S at sub-
116 nanomolar concentrations ($IC_{50} = 0.04$ nM (5.8 ng/mL); $IC_{90} = 0.3$ nM (44 ng/mL)), which was
117 similar or better than the parental IgGs and >100-fold better IC_{50} than the parental Fabs (Fig.1g).
118 Remarkably, CoV-X2 remained effective against pseudoviruses bearing escape mutations that
119 made them resistant to the individual mAbs (Fig.1g)¹⁴. We conclude that the *in vitro* binding and
120 neutralizing properties of CoV-X2 make it preferable over its parental antibodies.

121 To assess the clinical potential of CoV-X2, we investigated its ability to protect animals
 122 from infection and disease. We first developed a novel mouse model, in which human ACE2
 123 (hACE2) is expressed by upper and lower respiratory tract cells upon inhalation of a modified
 124 Adeno Associated Virus (AAV-hACE2, see Methods, Fig.2 and Extended Data Fig.6).



125
 126 **Fig.2 | CoV-X2 protects AAV-hACE2-transduced mice against SARS-CoV-2 disease.** a, Loss of body
 127 weight over time in SARS-CoV-2 infected mice. 13 to 15 weeks old C57Bl/6NcrJ wild type female mice

128 were transduced with AAV-hACE2 by forced inhalation, which provides delivery of viral particles to both
129 upper and lower respiratory tract. After >7 days, mice were either infected with SARS-CoV-2 (1×10^4 pfu)
130 or received vehiculum by the intranasal route. Weight was monitored daily for 8 days (SARS-CoV-2, $n =$
131 5; control, $n = 4$). Mean with standard deviation is shown. **b**, Kinetic of viral burden in the lungs from
132 SARS-CoV-2-infected mice by plaque assays. Mean with standard deviation; the dashed line indicates the
133 limit of detection. **c**, Kinetic of viral RNA levels in lung samples from SARS-CoV-2-infected mice by RT-
134 qPCR. Mean with standard deviation. **d**, Schematic of the experimental layout. Wild type mice were
135 transduced with AAV-hACE2 by forced inhalation. After >7 days, mice were inoculated intraperitoneally
136 (i.p) with 150 μg of antibodies. One day later, the mice were infected intranasally (i.n.) with SARS-CoV-2
137 (1×10^4 pfu). **e**, Changes in body weight upon infection were monitored daily in antibody-treated mice
138 (C121, $n=9$; C135, $n=5$; CoV-X2, $n=13$; isotype control, $n=10$). Mean with standard deviation is shown. **f**,
139 Lung viral burden by plaque assay at 5 dpi (isotype control, $n=6$; CoV-X2, $n=8$). The dashed line indicates
140 the limit of detection; mean with standard deviation. P value was calculated with two-tailed Student's t test.
141 **g**, Spleen viral RNA levels by RT-qPCR at 5 and 8 dpi (gray: isotype control; purple: CoV-X2). Mean with
142 standard deviation. P value was calculated with two-tailed Student's t test. **h**, Photographs of lungs collected
143 from infected mice (8 dpi). **i**, Histopathology. Hematoxylin and Eosin-stained sections of paraffin-
144 embedded lungs from infected mice (8 dpi). **j**, C121 treated mice developed an E484D mutation at the core
145 of the interface between RBD (yellow) and C121 heavy chain (HC, green) (PDB ID 7K8X). The
146 intermolecular interactions present in wild type and lost in E484D are shown.

147 This approach enables rapid production of large cohorts of animals and has the advantage of being
148 applicable to wild type and mutant mouse colonies, independently of age and gender. Moreover,
149 since AAV vectors are only weakly immunogenic and cytotoxic, the system allows for prolonged
150 expression of hACE2¹⁶⁻¹⁹ (Extended Data Fig.6). SARS-CoV-2 infection of ACE2 humanized
151 mice results in progressive weight loss, respiratory pathology and disease requiring culling on day
152 8 post infection (dpi, Fig.2a–c and Extended Data Fig.6).

153 To evaluate the protective effect of antibodies, hACE2 mice were treated with antibody
154 (150 μg) one day before SARS-CoV-2 challenge and monitored over time (Fig.2d–j). Upon
155 intranasal infection with 1×10^4 pfu of SARS-CoV-2 (SARS-CoV-2/human/Czech
156 Republic/951/2020), isotype control treated animals showed weight loss starting at 3 dpi, and by
157 8 dpi most animals had lost approximately 25–30% of their body weight reaching humane endpoint
158 (Fig.2e). Infectious virus could be recovered from the lungs (Fig.2f), and viral RNA was detected
159 also at distant tissues, such as spleen (Fig.2g). Lung pathology resembled severe COVID-19 in
160 humans²⁰ and was characterized by alveolar replacement with infiltrates of immune cells and

161 fibroblasts, thickened septa and activated macrophages with foamy cytoplasm in regions of
162 minimally changed morphology (Fig.2h,i and data not shown). In contrast, animals treated with
163 CoV-X2 maintained their body weight ($P < 0.0001$ on 4–8 dpi when compared to isotype; Fig.2e),
164 had reduced viral RNA in the spleen (Fig.2g) and displayed no macro- or histopathological
165 changes (Fig.2h,i). While infectious virus could be readily recovered from controls (5 of 6), it was
166 only recovered from 1 out of 8 CoV-X2 treated animals (Fig.2f). Therefore, CoV-X2 protects mice
167 from infection and disease.

168 Since monotherapy with C121 or C135 mAbs leads to virus escape *in vitro*¹⁴, we treated
169 hACE2 mice with the individual antibodies and sequenced the virus. Only wild type RBD
170 sequences were obtained from controls (n=10). Instead, the virus in mice treated with C121
171 acquired the mutation E484D (5 of 5 mice that were analyzed on 8 dpi). C121 escape mutations at
172 E484 were observed *in vitro*¹⁴. Mutations at this residue, present also in the novel South African
173 variant (501Y.V2), reduce neutralization by human sera more than 10-fold²¹. E484D affects
174 intermolecular H-bonds at the core of the C121/RBD interface (Fig.2j) and it is suggested to
175 increase the RBD affinity for ACE2²². Virus with D484 is pathogenic, since 7 out of 9 mice treated
176 with C121 developed disease (Fig.2e and data not shown). In contrast, and unlike the *in vitro*
177 results¹⁴, no virus evasion or pathology were observed in mice treated with C135 (n=5; Fig.2e and
178 data not shown). Similarly, none of the CoV-X2 treated animals (n=8) developed pathology, 6 had
179 wild type RBD sequence, one mouse had a mix of wild type and E484D/N440K sequences and
180 another a mix of wild type and E484D. Thus, in addition to protecting from disease, CoV-X2
181 suppresses virus escape.

182 Monoclonal antibodies targeting the SARS-CoV-2 S are in advanced clinical trials and
183 show promise against COVID-19^{1,2}. Concomitant use of multiple antibodies is preferred for

184 increased efficacy and added resistance against viral evasion. Indeed, the virus can escape pressure
185 by a single antibody *in vitro* and, as shown here, also in animals after only a few days from
186 infection. Moreover, RBD mutations threatening the efficacy of single monoclonals have already
187 been detected in virus circulating in minks and humans²³, including mutations at the C121 and
188 C135 epitopes (Extended Data Fig.7). One disadvantage of antibody cocktails is the requirement
189 for twice or more the production capacity than for single mAbs, which is a significant bottleneck
190 during the current pandemic.

191 Multispecific antibodies offer the advantages of cocktails in a single molecule. Indeed, we
192 have shown that the CoV-X2 bispecific is more effective than the related monoclonals at inhibiting
193 ACE2 binding; it has sub-nanomolar IC₅₀ against a broader array of viral sequences; and it protects
194 animals from SARS-CoV-2 even when C121, its potent parental mAb, fails due to the insurgence
195 of viral escape. C135, the other parental mAb, did not generate escape in our animal experiment
196 but readily generated them *in vitro*¹⁴. CoV-X2 is expected to be more resistant to viral escape
197 compared to monoclonals. Indeed, we have shown that CoV-X2 binds and neutralizes mutants not
198 recognized by its parental mAbs, including variants at and around the RBD residues mutated in
199 the recently emerging in the United Kingdom¹² and South Africa¹³ variants, which are associated
200 with faster spread and increased viral load.

201 CoV-X2 is an IgG-like molecule and as such could be further engineered to alter effector
202 functions. For example, the Fragment crystallizable (Fc) of CoV-X2 was already modified to
203 modulate its interaction with Fc receptors and complement (LALA-PG mutations)²⁴ without
204 affecting its antigen-binding properties. The LALA modification prevents Antibody Dependent
205 Enhancement (ADE) of flavivirus infection^{25,26} and it may be a desirable modification also in the
206 context of SARS-CoV-2, since ADE was reported in cellular and animal experiments with

207 coronaviruses, including SARS-CoV²⁷⁻²⁹. Other modifications, like LS²⁴ for increased half-life,
208 are easily achievable. Finally, CoV-X2 is human-derived and produced in a format (CrossMab)
209 already shown to be safe in clinical trials³⁰, which further supports its developability. Thus, IgG-
210 like bispecifics are worth adding to the arsenal employed to combat SARS-CoV-2 and its plausible
211 future mutations.

212

213 **References:**

- 214 1 DeFrancesco, L. COVID-19 antibodies on trial. *Nat Biotechnol* **38**, 1242-1252,
215 doi:10.1038/s41587-020-0732-8 (2020).
- 216 2 Klasse, P. J. & Moore, J. P. Antibodies to SARS-CoV-2 and their potential for
217 therapeutic passive immunization. *Elife* **9**, doi:10.7554/eLife.57877 (2020).
- 218 3 Robbiani, D. F. *et al.* Convergent antibody responses to SARS-CoV-2 in convalescent
219 individuals. *Nature* **584**, 437-442, doi:10.1038/s41586-020-2456-9 (2020).
- 220 4 Baum, A. *et al.* REGN-COV2 antibodies prevent and treat SARS-CoV-2 infection in
221 rhesus macaques and hamsters. *Science* **370**, 1110-1115, doi:10.1126/science.abe2402
222 (2020).
- 223 5 Schäfer, A. *et al.* Antibody potency, effector function, and combinations in protection
224 and therapy for SARS-CoV-2 infection in vivo. *Journal of Experimental Medicine* **218**,
225 doi:10.1084/jem.20201993 (2020).
- 226 6 Schlake, T. *et al.* mRNA: A Novel Avenue to Antibody Therapy? *Mol Ther* **27**, 773-784,
227 doi:10.1016/j.ymthe.2019.03.002 (2019).
- 228 7 Tiwari, P. M. *et al.* Engineered mRNA-expressed antibodies prevent respiratory syncytial
229 virus infection. *Nature communications* **9**, 3999, doi:10.1038/s41467-018-06508-3
230 (2018).
- 231 8 Rybakova, Y. *et al.* mRNA Delivery for Therapeutic Anti-HER2 Antibody Expression
232 In Vivo. *Mol Ther* **27**, 1415-1423, doi:10.1016/j.ymthe.2019.05.012 (2019).
- 233 9 Barnes, C. O. *et al.* SARS-CoV-2 neutralizing antibody structures inform therapeutic
234 strategies. *Nature*, doi:10.1038/s41586-020-2852-1 (2020).
- 235 10 Schaefer, W. *et al.* Immunoglobulin domain crossover as a generic approach for the
236 production of bispecific IgG antibodies. *Proc Natl Acad Sci U S A* **108**, 11187-11192,
237 doi:10.1073/pnas.1019002108 (2011).
- 238 11 Walls, A. C. *et al.* Structure, Function, and Antigenicity of the SARS-CoV-2 Spike
239 Glycoprotein. *Cell* **181**, 281-292.e286, doi:10.1016/j.cell.2020.02.058 (2020).
- 240 12 Kemp, S. *et al.* Recurrent emergence and transmission of a SARS-CoV-2 Spike deletion
241 Δ H69/V70. *bioRxiv*, 2020.2012.2014.422555, doi:10.1101/2020.12.14.422555 (2020).
- 242 13 Tegally, H. *et al.* Emergence and rapid spread of a new severe acute respiratory
243 syndrome-related coronavirus 2 (SARS-CoV-2) lineage with multiple spike mutations in
244 South Africa. *medRxiv*, 2020.2012.2021.20248640, doi:10.1101/2020.12.21.20248640
245 (2020).

- 246 14 Weisblum, Y. *et al.* Escape from neutralizing antibodies by SARS-CoV-2 spike protein
247 variants. *eLife* **9**, e61312, doi:10.7554/eLife.61312 (2020).
- 248 15 Schmidt, F. *et al.* Measuring SARS-CoV-2 neutralizing antibody activity using
249 pseudotyped and chimeric viruses. *J Exp Med* **217**, doi:10.1084/jem.20201181 (2020).
- 250 16 Han, K. *et al.* Lung Expression of Human ACE2 Sensitizes the Mouse to SARS-CoV-2
251 Infection. *Am J Respir Cell Mol Biol*, doi:10.1165/rcmb.2020-0354OC (2020).
- 252 17 Hassan, A. O. *et al.* A SARS-CoV-2 Infection Model in Mice Demonstrates Protection
253 by Neutralizing Antibodies. *Cell* **182**, 744-753.e744, doi:10.1016/j.cell.2020.06.011
254 (2020).
- 255 18 Sun, J. *et al.* Generation of a Broadly Useful Model for COVID-19 Pathogenesis,
256 Vaccination, and Treatment. *Cell* **182**, 734-743.e735, doi:10.1016/j.cell.2020.06.010
257 (2020).
- 258 19 Sun, S. H. *et al.* A Mouse Model of SARS-CoV-2 Infection and Pathogenesis. *Cell Host*
259 *Microbe* **28**, 124-133.e124, doi:10.1016/j.chom.2020.05.020 (2020).
- 260 20 Deshmukh, V., Motwani, R., Kumar, A., Kumari, C. & Raza, K. Histopathological
261 observations in COVID-19: a systematic review. *Journal of clinical pathology*, jclinpath-
262 2020-206995, doi:10.1136/jclinpath-2020-206995 (2020).
- 263 21 Greaney, A. J. *et al.* Comprehensive mapping of mutations to the SARS-CoV-2 receptor-
264 binding domain that affect recognition by polyclonal human serum antibodies. *bioRxiv*,
265 2020.2012.2031.425021, doi:10.1101/2020.12.31.425021 (2021).
- 266 22 Chen, J., Wang, R., Wang, M. & Wei, G. W. Mutations Strengthened SARS-CoV-2
267 Infectivity. *J Mol Biol* **432**, 5212-5226, doi:10.1016/j.jmb.2020.07.009 (2020).
- 268 23 Weisblum, Y. *et al.* Escape from neutralizing antibodies by SARS-CoV-2 spike protein
269 variants. *Elife* **9**, doi:10.7554/eLife.61312 (2020).
- 270 24 Saunders, K. O. Conceptual Approaches to Modulating Antibody Effector Functions and
271 Circulation Half-Life. *Frontiers in immunology* **10**, 1296,
272 doi:10.3389/fimmu.2019.01296 (2019).
- 273 25 Dejnirattisai, W. *et al.* Cross-reacting antibodies enhance dengue virus infection in
274 humans. *Science* **328**, 745-748, doi:10.1126/science.1185181 [pii]
275 10.1126/science.1185181 (2010).
- 276 26 Sridhar, S. *et al.* Effect of Dengue Serostatus on Dengue Vaccine Safety and Efficacy. *N*
277 *Engl J Med* **379**, 327-340, doi:10.1056/NEJMoa1800820 (2018).
- 278 27 Yip, M. S. *et al.* Antibody-dependent infection of human macrophages by severe acute
279 respiratory syndrome coronavirus. *Virology* **11**, 82, doi:10.1186/1743-422x-11-82 (2014).
- 280 28 Jaume, M. *et al.* Anti-severe acute respiratory syndrome coronavirus spike antibodies
281 trigger infection of human immune cells via a pH- and cysteine protease-independent
282 FcγR pathway. *J Virol* **85**, 10582-10597, doi:10.1128/jvi.00671-11 (2011).
- 283 29 Yip, M. S. *et al.* Antibody-dependent enhancement of SARS coronavirus infection and its
284 role in the pathogenesis of SARS. *Hong Kong Med J* **22**, 25-31 (2016).
- 285 30 Klein, C. *et al.* Engineering therapeutic bispecific antibodies using CrossMab technology.
286 *Methods* **154**, 21-31, doi:10.1016/j.ymeth.2018.11.008 (2019).
- 287

288 **Acknowledgements**

289 *Dedicated to the memory of the recently departed Prof. François Diederich.*

290 This work was supported by: the European Union's Horizon 2020 research and innovation
291 program under grant agreement No. 101015756, ATAC consortium (EC 101003650; D.F.R., L.V.,
292 Q.P.H., F.B., L.C.); SNF grant 31003A_182270 (L.V.); Lions Club Monteceneri (L.V.); George
293 Mason University Fast Grant (D.F.R.); NIH grant P01-AI138398-S1 (M.C.N., P.J.B.);
294 2U19AI111825 (M.C.N., D.F.R.); the Caltech Merkin Institute for Translational Research and P50
295 AI150464 (P.J.B.); R37-AI64003 (P.D.B.); R01AI78788 (T.H.); P.D.B. and M.C.N. are Howard
296 Hughes Medical Institute Investigators. The study was also supported by: the Czech Academy of
297 Sciences and Czech Ministry of Agriculture (RVO 68378050; R.S.; RVO0518; D.R.); Czech
298 Ministry of Education, Youth and Sports and the European Regional Development Fund
299 (LM2018126; CZ.1.05/2.1.00/19.0395 and CZ.1.05/1.1.00/02.0109; R.S.;
300 CZ.02.1.01/0.0/0.0/15_003/0000495; D.R.); and Czech Science Foundation (20-14325S, D.R.).
301 We are grateful for the high-performance computing resources provided by CINECA, Dr. Sanzio
302 Bassini, to Prof. Michael Hust, Dr. Federico Bertoglio and Elisa Restivo. We thank Vaclav
303 Zatecka, Veronika Martinkova, and Linda Kutlikova for technical assistance.

304

305 **Author contributions**

306 R.D.G, M.Pe., L.S., F.Mu., J.C.L., F.Ma, D.M., C.I., E.P., S.D.G., M.Pa., F.B., D.M., S.Gi., C.O.B,
307 F.B., J.C.S, F.G, S.Ga, designed and carried out experiments and analyzed results, produced
308 plasmids, antibodies and viral proteins. P.N., T,M., J.H., V.H, B.M., N.P., A.F., J.T., V.I., M.Pa.,
309 D.Z., P.B., I.B., P.S., D.R., performed animal experiments and analyzed the results. L.V, D.F.R.,
310 D.R., Q.P.H., A.P., L.C., P.J.B., M.C.N., P.D.B., T.H. conceived and designed study and

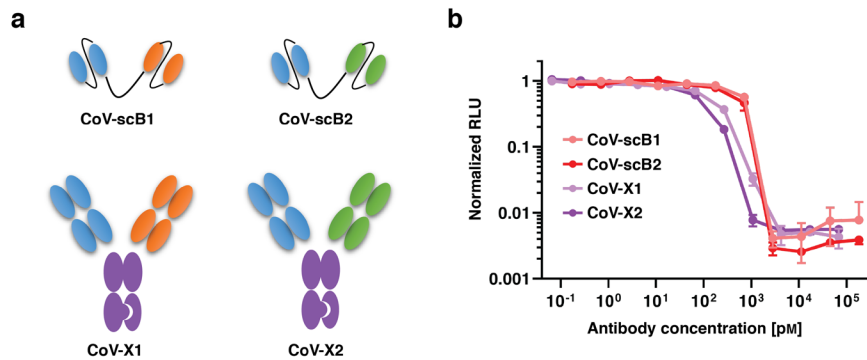
311 experiments and analyzed the results. P.N., R.N., O.P., J.P., J.R., R.S. conceived and designed the
312 mouse model. L.V., D.F.R., D.R, R.D.G. wrote the manuscript with input from all co-authors.

313 **Competing interests**

314 In connection with this work the Institute for Research in Biomedicine has filed a provisional
315 patent application on which L.V. is inventor (PCT/EP2020/085342). The Rockefeller University
316 has filed a provisional patent application on which D.F.R. and M.C.N. are inventors.

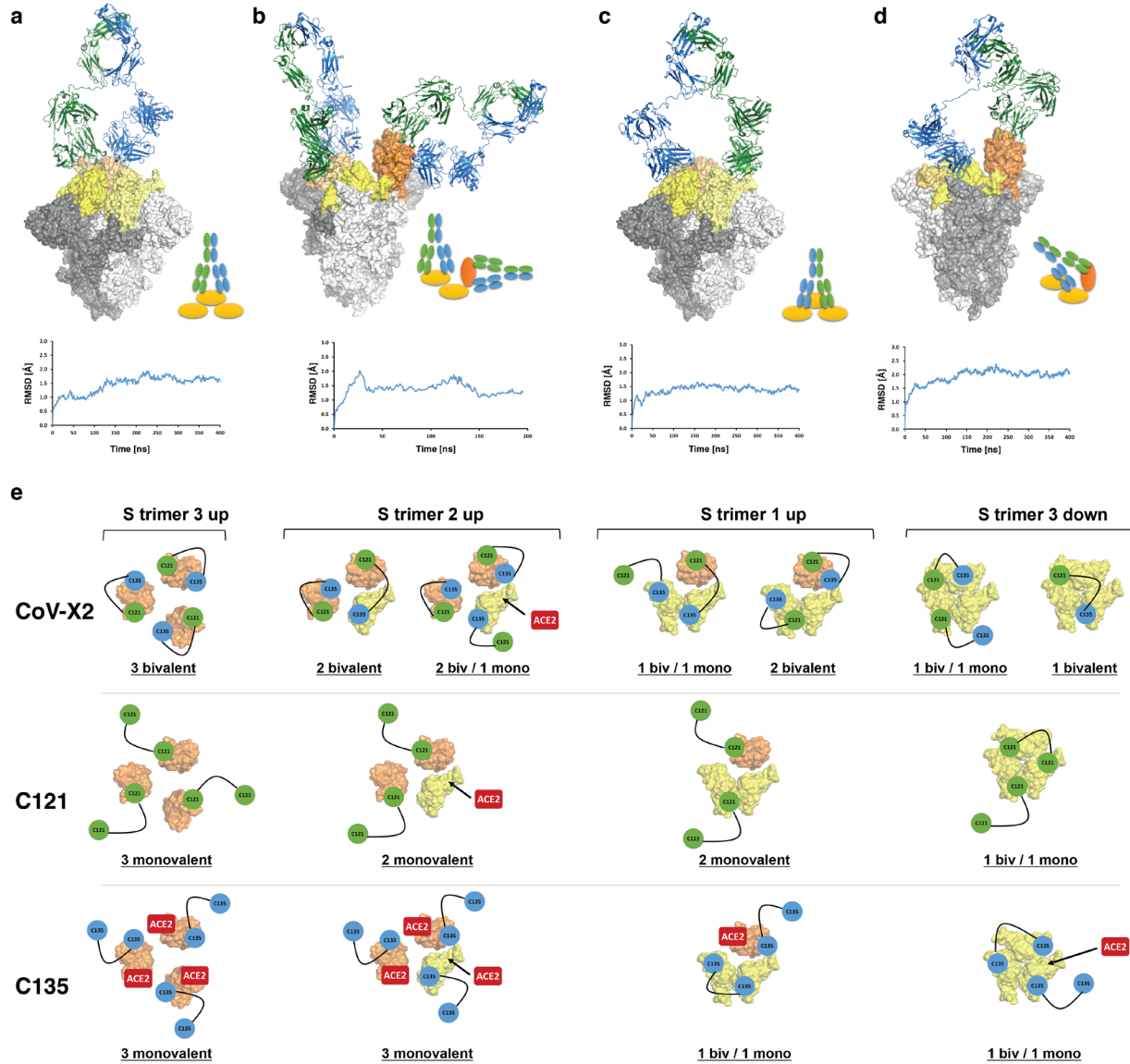
317

318 **Extended data figures**



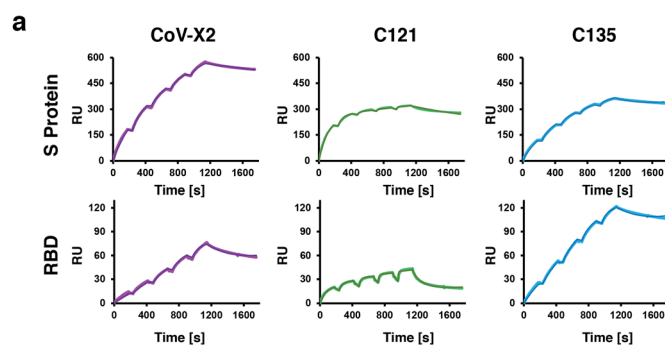
319

320 **Extended Data Fig.1 | Neutralization of SARS-CoV-2 pseudovirus by bispecific antibodies. a,**
321 Schematic representation of the 4 bispecific constructs; two in scFv format and two as IgG-like CrossMAb
322 with knob-in-hole. The parental monoclonals forming the bispecifics are color-coded (C135 blue, C144
323 orange, C121 green; Fc region in purple). **b,** All 4 constructs neutralize SARS-CoV-2 pseudovirus *in vitro*
324 at sub-nanomolar concentrations (IC_{50} : 0.13, 0.04, 0.74 and 0.53 nM for CoV-X1, CoV-X2, CoV-scB1 and
325 CoV-scB2, respectively). Normalized relative luminescence values, which correlate to infection, are
326 reported versus antibody concentration, as detailed in Schmidt *et al.*¹⁵. Mean with standard deviation is
327 shown, representative of two independent experiments.



328

329 **Extended Data Fig.2 | CoV-X2 engages its epitopes on all RBD conformations on the S trimer. a–d,**
 330 Molecular Dynamics (MD) simulations of the complex between the CoV-X2 bispecific and S trimers with
 331 RBD in either all down, all up or mixed up/down conformations show that CoV-X2 can engage a single
 332 RBD with both arms (**a,b**), two adjacent RBDs in the down conformation (**c**), and two RBDs in the up/down
 333 conformation (**b,d**). The complexes were subjected to up to 400 ns of fully atomistic MD simulations to
 334 assess feasibility and stability of the bound conformations. Root-mean-squared deviations (RMSD) values
 335 are shown to indicate structural stability. S trimer is in shades of grey, RBDs in yellow (down conformation)
 336 and orange (up), the C121 and C135 moieties of CoV-X2 are in green and blue, respectively. **e**, Schematic
 337 representation of the computationally predicted binding modes of CoV-X2, C121 IgG and C135 IgG on the
 338 S trimer, colored as in **a–d**. Antibodies are represented by connected circles; ACE2 is in red on the RBD if
 339 it can bind directly to a given conformation; it has an arrow pointing to the RBD if ACE2 binding is
 340 achieved after an allowed switch to the up conformation. For example, in the 3-up conformation (left),
 341 CoV-X2 can engage all the RBDs with bivalent binding, whereas C121 and C135 can only achieve
 342 monovalent binding. C135 binding does not prevent interaction with ACE2. The situation is similar in the
 343 other S conformations (2-up 1-down, 2-down 1-up and 3-down), with only the bispecific achieving bivalent
 344 interaction and preventing ACE2 access in all conformations.

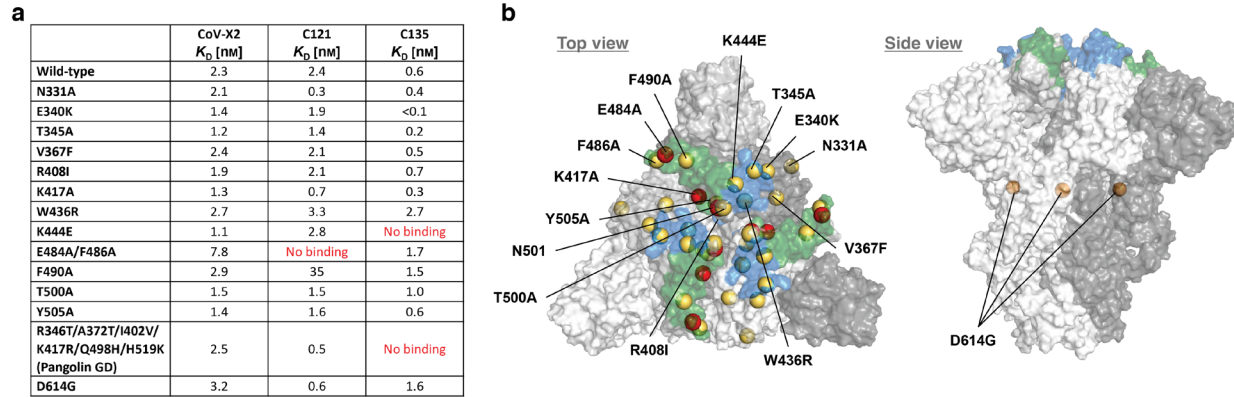


b

		CoV-X2	C121	C135
Spike protein	k_a [$\cdot 10^6 \text{ M}^{-1} \text{ s}^{-1}$]	0.69	1.33	0.62
	k_d [$\cdot 10^{-3} \text{ s}^{-1}$]	0.12	0.17	0.13
	K_D [nM]	0.18	0.13	0.21
RBD	k_a [$\cdot 10^6 \text{ M}^{-1} \text{ s}^{-1}$]	0.58	1.30	0.20
	k_d [$\cdot 10^{-3} \text{ s}^{-1}$]	1.35	3.15	0.12
	K_D [nM]	2.35	2.40	0.59

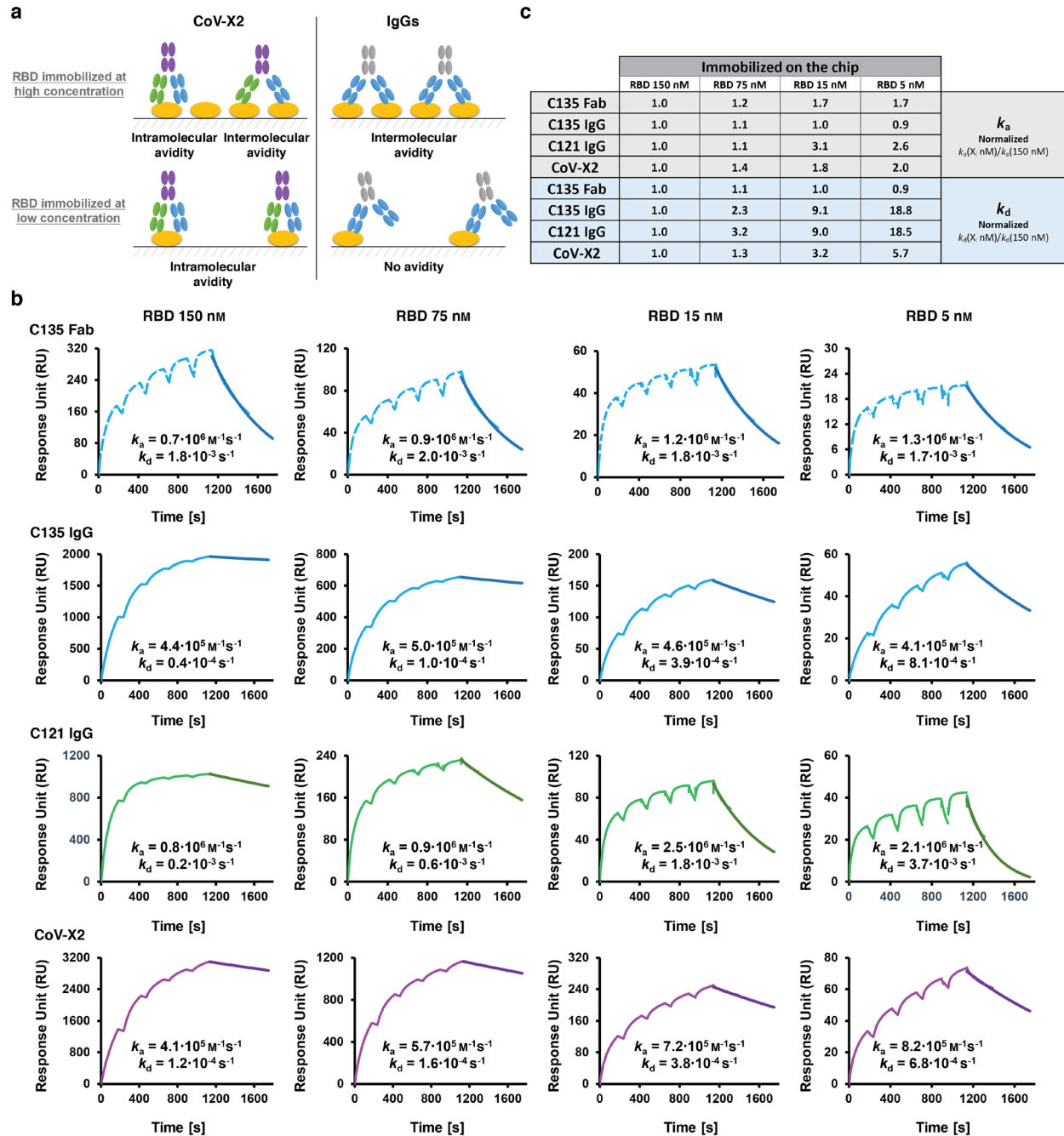
345

346 **Extended Data Fig.3 | CoV-X2 and its parental mAbs bind recombinant, isolated RBD and S trimer**
 347 **with low nanomolar affinity. a,** Representative SPR traces from which the data in (b) was derived. **b,**
 348 Kinetic parameters for the binding of C121 IgG, C135 IgG, and CoV-X2 to S trimer and RBD.



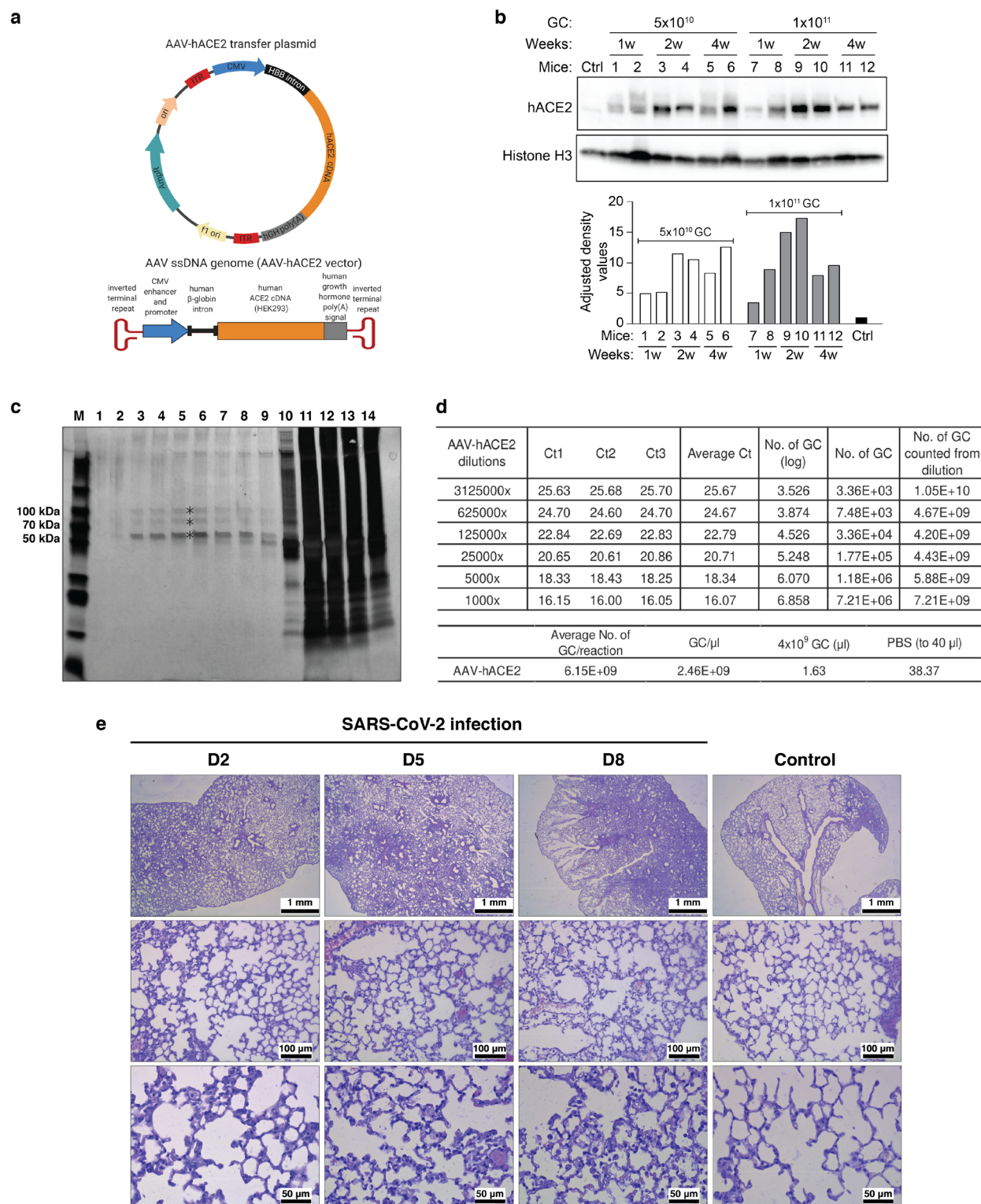
349

350 **Extended Data Fig.4 | CoV-X2 binds with low-nanomolar affinity to S protein mutants, including**
 351 **some that are not recognized by the parental mAbs C121 and C135. a, SPR-derived binding affinities**
 352 **of CoV-X2, C121 IgG and C135 IgG to several S trimer mutants. b, Mutations tested in (a) are indicated**
 353 **by yellow spheres on the surface representation of the S trimer. Residues mutated in the circulating**
 354 **501Y.V2 variant with increased spread and viral load are in red. The epitopes of C121 (green) and C135**
 355 **(blue) are shown.**



356
 357 **Extended Data Fig.5 | SPR-based avidity assays confirm that CoV-X2 can engage bivalently on a**
 358 **single RBD.** **a**, CoV-X2 and monoclonal IgGs (C121 or C135) have different binding modes available
 359 when high or low quantities of RBD are immobilized on the surface of the SPR chip. mAbs have avidity
 360 effects at high RBD concentrations due to intermolecular binding, which results in slower dissociation rate
 361 (k_d), but not at low RBD concentrations, since bivalent binding to a single RBD is impossible. In contrast,
 362 the bispecific has avidity at both high and low concentrations, since bivalent binding to its two epitopes on
 363 a single RBD is possible. k_a is not affected by avidity. **b**, Experimental confirmation that CoV-X2 engages
 364 bivalently on a single RBD. SPR traces used to determine k_a and k_d of mAbs, Fab and bispecific at different
 365 concentrations of immobilized RBD (see Fig.1d) are shown. **c**, Table summarizing the SPR results plotted
 366 in Fig.1d. k_a and k_d were normalized against the values at the highest RBD concentration. k_a and Fab k_d were

367 unaffected by the RBD concentration, as expected. k_d became faster for the monoclonals (loss of avidity)
368 but less so for the bispecific (avidity maintained due to simultaneous binding to two sites on a single RBD).

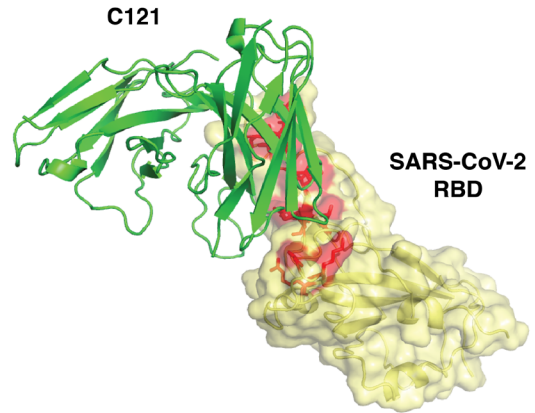


369
 370 **Extended Data Fig.6 | Generation of the new AAV-hACE2-transduced mouse model for COVID-19.**
 371 **a**, Diagram of the AAV-hACE2 plasmid and corresponding Adeno Associated viral vector. **b**, Western blot
 372 analysis detecting hACE2 expression in the lungs of one non-transduced control mouse (Ctrl) and 12 mice
 373 transduced with two different doses of AAV-hACE2 viral particles (5×10^{10} or 1×10^{11} genome copies (GC)).
 374 Lung tissue was collected 1, 2, or 4 weeks (w) post transduction. Histone H3 was used as control for

375 quantification (bottom). **c**, Preparation of concentrated AAV-hACE2. AAV-hACE2 plasmid was co-
376 transfected with pHelper and AAV Rep/Cap 2/9n vectors into 293AAV cells (see Methods). In order to
377 increase viral titers, viral particles from both cell lysate and PEG-precipitated growth medium were
378 ultracentrifuged in discontinuous iodixanol gradient. The silver-stained SDS-PAGE gel shows 14
379 consecutive fractions: 1-9 represent enriched AAV fractions used for experiments, whereas fractions 10–
380 14 are contaminated with proteinaceous cell debris. Iodixanol was chosen as a density gradient medium
381 due to its low toxicity *in vivo* and its easy removal by ultrafiltration. M is protein marker, * are AAV capsid
382 proteins VP1, VP2, and VP3. **d**, The amount of AAV particles was estimated by qRT-PCR. The number of
383 genome copies (GC) expressed as log was calculated from a standard curve. From one 15 cm² dish, 75 μl
384 with 2.0x10¹² GC/ml were prepared, which is sufficient for hACE2 humanization of 37 mice. **e**, Kinetic of
385 lung histopathology in SARS-CoV-2 infected ACE2 humanized mice. Hematoxylin and Eosin stained
386 sections showed inflammatory infiltrates composed of lymphocytes, macrophages, neutrophils, and
387 fibroblasts replacing the alveoli. The size of the affected areas increased over time. Alveolar septa were
388 thickened in areas close to infiltrates. In samples collected at 5 and 8 dpi, an increased number of activated
389 macrophages with foamy cytoplasm was seen in regions with minimally changed morphology. AAV-
390 hACE2 transduced, SARS-CoV-2 uninfected mice were used as control and showed no significant
391 pathology.

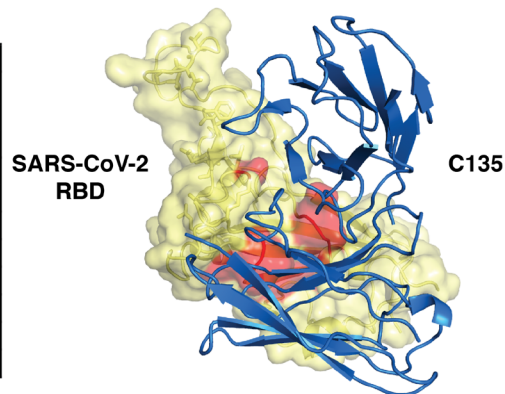
a

wt	mutant	Strain Name	wt	mutant	Strain Name
Arg403	Lys	/USA/VA-DCLS-0630/2020 /USA/VA-DCLS-0439/2020 /AUS/VIC1787/2020	Gly485	Arg	/AUS/VIC1829/2020 /AUS/VIC1960/2020 /AUS/VIC1693/2020 /AUS/VIC1660/2020 /AUS/VIC1683/2020 /AUS/VIC1588/2020 /AUS/VIC1565/2020 /AUS/VIC1611/2020 /AUS/VIC1812/2020 /AUS/VIC2023/2020
Lys444	Asn	/AUS/VIC4515/2020			
Gly446	Asp	/USA/FL-BPHL-2211/2020			
	Val	/USA/MN-MDH-1430/2020 /AUS/VIC913/2020 /AUS/VIC6087/2020 /AUS/VIC9542/2020			
Leu452	Gln	/USA/VA-DCLS-1404/2020	Cys488	Arg	/IRN/COVID19-IRVSH4/2020
	Arg	/USA/CA-CZB-12872/2020	Phe490	Leu	/AUS/VIC10024/2020 /AUS/VIC766/2020
	Met	/BHR/340798279_55_L001/2020 /USA/CA-CZB-1043/2020 /IND/906/2020		Pro491	His
Leu455	Phe	/AUS/VIC10121/2020 /AUS/VIC5196/2020	Gln493	Leu	/USA/WI-UW-371/2020
Val483	Ala	/USA/WA-UW-6527/2020 /USA/WA-UW-1587/2020 /USA/WA-RML-2/2020 /USA/WA-RML-6/2020 /USA/WA-RML-5/2020 /USA/UT-03764/2020	Ser494	Pro	/USA/CA-CZB-4047/2020 /USA/CA-CZB-11677/2020 /USA/CA-CZB-6994/2020 /USA/CA-CZB-11010/2020 /USA/MI-MDHHS-SC20047/2020 /USA/CA-CZB-12810/2020 /AUS/VIC9505/2020
		Phe			/AUS/VIC2139/2020 /USA/MA-UW-629/2020
	Glu484	Gln			/USA/UT-UPHL-2009538/2020 /IND/GBRC278a/2020 /USA/SEARCH-1462-SAN/2020
Lys		/USA/UT-QDX-1869/2020 /BHR/340859913_511/2020 /USA/IL-UW-379/2020			
Ala		/USA/VA-DCLS-1615/2020			



b

wt	mutant	Strain Name
Phe342	Leu	England/01_1/29
Ala344	Ser	/USA/WA-S2278/2020 /USA/WA-S2530/2020
	Thr	/IND/GBRC431a/2020
	Val	/AUS/VIC10958/2020
Thr345	Ser	/USA/WA-S1049/2020
	Ile	/PER/covper051/2020
Arg346	Thr	/IND/GBRC333/2020
Trp436	Thr	/IND/GBRC333/2020
Asn439	Lys	/USA/L-UW/799/2020
Asn440	Lys	/HKG/Case5138/2020
Leu441	Ile	/USA/FL-BPHL-0297/2020
Asn450	Lys	/IND/906/2020



392
393
394
395
396

Extended Data Fig.7 | Natural SARS-CoV-2 variants in the C121 and C135 epitopes. Summary of naturally occurring mutations in the C121 (a) or C135 (b) epitopes reported in circulating SARS-CoV-2 (as of January 1, 2021). The location of the mutated residues is shown in red on the RBD structure. C121 and C135 variable regions are in green and blue (PDB ID: 7K8X and 7K8Z respectively).